AIAA JOURNAL
Vol. 46, No. 12, December 2008

Disturbances Growth in Boundary Layers on Classical and Wavy Surface Wings

Ilya Zverkov,* Boris Zanin,† and Viktor Kozlov‡
Russian Academy of Sciences, 630090, Novosibirsk, Russia

DOI: 10.2514/1.37562

Oil-film visualization patterns of the flow on a classical wing and on a wing with a wavy surface at various angles of attack are analyzed. For low Reynolds numbers ($Re < 2 \times 10^5$), the boundary-layer structure on a wavy wing is demonstrated to differ significantly from that on a classical wing. As a result, leading-edge stall on a wavy wing occurs later than on a smooth wing. The present activities form the basis for a systematic study of the boundary-layer structure on a wavy wing. For this purpose, a series of investigations is performed. Boundary-layer parameters on classical and wavy-surface wings at the angle of attack $\alpha = 0$ deg and the chord Reynolds number $Re = 1.7 \times 10^5$ are studied experimentally. The combined experiment includes oil-film visualization, measurements of pressure distributions, and flow velocity. On both wings, substantial differences are found in the transition position and in the transition scenarios realized on the wavy-surface wing along its streamwise grooves and humps. However, some similarity in the disturbance growth in both separation-bubble regions is found.

Nomenclature

b	=	maximum wing thickness
C_p	=	pressure coefficient, $(p - p_0)/q + 1$
c	=	airfoil chord length
E	=	voltage from hot-wire anemometer
F	=	frequency
f	=	hump height
g	=	hump width
H_{12}	=	shape factor, δ_1/δ_2
H_{32}	=	shape factor, δ_3/δ_2
h	=	distance between surface and separated shear layer in Green's profiles
k_1, k_2	=	empirical constants for hot-wire calibration
L	=	wingspan
l	=	shear-layer thickness in Green's two-parameter velocity profiles
n	=	empirical constant for hot-wire calibration
p	=	static pressure on the model surface
p_0	=	total pressure
q	=	mean freestream dynamic pressure
Re	=	chord Reynolds number
r	=	hump curvature radius
s	=	bubble length
Tu	=	freestream turbulence level, % from U_∞
U_e	=	mean external velocity
U_∞	=	mean freestream velocity
u	=	local mean (tangential) velocity
v	=	groove width
x	=	distance along the airfoil chord
y	=	distance normal to the airfoil surface
z	=	distance along the wingspan
δ	=	boundary-layer thickness
δ_1	=	boundary-layer displacement thickness, $\int_0^\delta (1 - u/U_e)\,dy$
δ_2	=	boundary-layer momentum thickness, $\int_0^\delta (u/U_e)(1 - u/U_e)\,dy$
δ_3	=	boundary-layer energy thickness, $\int_0^\delta (u/U_e)[1 - (u/U_e)^2]\,dy$
ξ	=	deviation of calculated velocity profile from experimental velocity profile

Subscripts

c	=	center of wave packet
cl	=	classical-wing boundary layer
e	=	external to boundary layer
gr	=	wavy-wing boundary layer along a groove
∞	=	freestream condition
0	=	zero local mean velocity

Received 17 March 2008; accepted for publication 6 August 2008.

*Senior Research Scientist, Khristianovich Institute of Theoretical and Applied Mechanics, Siberian Branch, Institutskaya 4/1.

†Leading Senior Research Scientist, Khristianovich Institute of Theoretical and Applied Mechanics, Siberian Branch, Institutskaya 4/1.

‡Head of Laboratory, Khristianovich Institute of Theoretical and Applied Mechanics, Siberian Branch, Institutskaya 4/1.

I. Introduction

NOWADAYS, micro air vehicles (MAVs) find new military and civil applications. Miniaturization of the electronic equipment promotes the creation of progressively smaller unmanned aircraft [1]. At the moment, many researchers pay much attention to MAVs with an overall mass below 0.5 kg and a chord-based Reynolds number between 10^4 and 10^5 [2]. In spite of certain success, the wide application of MAVs is limited by their rather modest aerodynamic performances. Important MAV parameters, such as the critical angle of attack and lift-to-drag ratio, are mainly deteriorated by changes in the boundary-layer flow character at low Reynolds numbers. The flow separation on the wing surface and interrelation between the separation and laminar-turbulent transition start to play a more significant role within the Reynolds numbers range from 10^4 to 10^5. In this range, the boundary-layer separation necessarily exists, either on one side or another of a wing with a relative thickness of more than 0.1 chord at any angle of attack, because the laminar boundary layer keeps on to the adverse pressure gradient area and then separates [3–5]. At higher angles of attack, the flow separation point approaches the wing leading edge. The transition from a laminar to a turbulent flow occurs in this separation region. The boundary-layer structure on the classical wing at low Reynolds numbers has been thoroughly investigated by various methods [3–9]. Figure 1 shows a layout of such a boundary layer.

Some nonprofit software products are available for calculating a two-dimensional flow past an airfoil, including the influence of the boundary layer and the Reynolds number [10,11]. As is clear from

the cited papers, one of the primary factors providing a crucial effect on lift, drag, etc., is the flow separation location and large-scale regions of the separated flow. Such flow regimes appear in a wide range of angles of attack, in particular, on wings with a large relative thickness. Aerodynamic characteristics of a wing can be modified by a separation-control system, which is either able to initiate or to prevent the flow separation. Wing surface modification is one of the major resources of separation control and aerodynamic performance improvement. It has been demonstrated that the turbulent boundary-layer structure at low Reynolds numbers is three-dimensional [12–15]. It has also been shown that it is possible to affect the flow structure by three-dimensional vortices, for example, setting a local hump in the separation region [16]. The next reasonable step is to consider the effect of spanwise-periodic modifications to the wing surface on the laminar boundary-layer separation. In the present paper, we use two terms that are understood as follows. The classical wing is a wing whose spanwise surface curvature radius is larger than the curvature radius near the leading edge by several orders of magnitude. The wavy surface or simply wavy wing is a wing whose spanwise surface consists of alternating humps and grooves forming an arbitrary configuration in the general case. Particular geometric parameters of humps and grooves are given in the paper.

Three aspects of wavy-wing research can be distinguished. First, such a wavy wing has already been used in practice for a rather long time as ram-air parachutes and paragliders. In those cases, the wing surface is not rigid, but is manufactured of an airtight fabric. The boundary layer on such wings was studied, for example, by Babinski [17,18], who investigated a paraglider wing section. The air inlets were located on the leading edge of such a wing. During the flight, the wing surface acquired a specific form with certain spanwise waviness. In his papers, Babinski noted that the paraglider wing characteristics were worse than those of the classical wing. A possible reason, however, is the presence of the air inlet on the wing leading edge.

The second aspect is the study of the wing with waviness near the leading edge only. A prototype of such a wing was a humpback whale flipper. Fish and Battle [19] reported that the flippers have a large aspect ratio (about six), and large-scale protuberances are present on the leading edge. The flipper cross section has a profile similar to the NACA 63_4–021 airfoil. The amplitude of leading-edge protuberances ranges from 2.5 to 12% of the chord, with a spanwise extent of 10–50% of the chord, depending on the spanwise location. Watts and Fish [20] and Fish and Lauder [21] examined the performance of a low-aspect-ratio wing with leading-edge hump numerically using panel methods and showed that, at an angle of attack $\alpha = 10$ deg, the lift increases by 4.8% over the classical wing. Subsequently, Miklosovic et al. [22] investigated the lift and drag of humpback whale flipper models in a wind tunnel. Their study considered tapered wings with an aspect ratio approximating that of a whale flipper. They reported a 6% increase in maximum lift over the classical wing and a delay of the stall angle of attack by about 40% for a flipper model with a humpback leading edge. Johari et al. [23] published a recent paper with a detailed study of the influence of leading-edge hump parameters on the aerodynamic characteristics of the wing. They studied three hump amplitudes (0.025, 0.5, and $0.12c$) and two wavelengths (0.25 and $0.5c$) and noted that the hump wavelength exerts only a weak effect on the wing performance. An increase in the hump amplitude yields a lower maximum lift force and a higher critical angle of attack. As a consequence, the lift curve is flattened. Van Nierop et al. [24] made an attempt to explain the influence of the humps on the leading edge on lift-curve flattening via local parameters of the turbulent boundary layer. They assumed that the turbulent boundary layer in the groove, because of a higher positive pressure gradient, separated earlier than on the hump. On the other hand, the associated gradual decrease in flow downwash leads to a stall delay. A common feature of these publications is to consider the effect of surface waviness on stall as a consequence of separation of the turbulent boundary layer [24].

Our previous work [25] presents the third aspect of wavy-wing research. In our case, the hump is extended along the entire chord of the wing, as on a paraglider. The hump height is $0.01c$ and the spanwise wavelength is $0.125c$. Other important parameters worth mentioning are the Reynolds number, which was 1.7×10^5, and the low degree of freestream turbulence ($Tu < 0.04\%$). Under such conditions, stall on the classical wing occurs via the bursting of a laminar separation bubble [3], rather than via the development of the turbulent boundary-layer separation. In this case, as was demonstrated [25], the stall angle of attack of the wavy wing is 1.5 times that of the classical wing and turbulent boundary-layer separation was not observed. However, it is still unknown what kind of disturbances are generated in the boundary layer by the surface waviness.

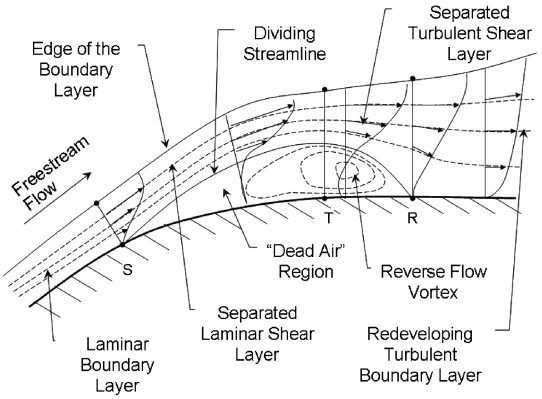

Fig. 1 Flow in the vicinity of a transitional separation bubble [5].

The present paper describes a further detailed qualitative and quantitative investigation of the boundary layer on the classical and wavy wings. A comprehensive study combined oil-film visualization with measurements of pressure distributions and velocity. The oil-film visualization showed the difference in the separation-region locations on the classical and wavy wings, and the hot-wire anemometry captured the differences in scenarios and positions of the laminar-turbulent transition.

II. Experimental Apparatus

A. Wind Tunnel

All experiments were performed in a T-324 subsonic wind tunnel based at the Khristianovich Institute of Theoretical and Applied Mechanics of the Siberian Branch of the Russian Academy of Sciences. This is a closed-circuit wind tunnel shown schematically in Fig. 2. There are nine screens in the wind-tunnel convergent channel to reduce the turbulence level. The contraction ratio of the convergent channel is 16:1. The turbulence level measured by a single I-type hot-wire anemometer sensor is lower than 0.04% in the frequency range of 1–5000 Hz [26]. The freestream velocity is $U_\infty = 12$ m/s, and the chord-based Reynolds number is $Re = 1.7 \times 10^5$.

The wind tunnel is equipped with a three-component, computer-controlled traverse mechanism. The traverse system has a resolution of 0.005 mm in the chordwise direction, 0.005 mm in the spanwise

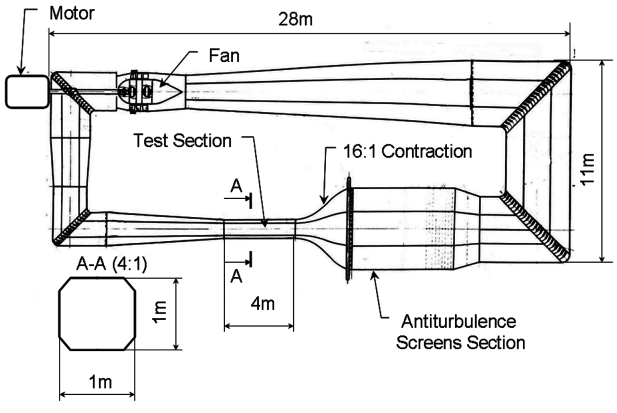

Fig. 2 Sketch of T-324 wind tunnel.

direction, and 0.0025 mm in the surface-normal direction. Both the hot-wire anemometer sensor and the static pressure probe could be traversed.

B. Models

Two wing models with a 195 mm chord and a 200 mm span were used in the experiments. The fiberglass models were painted black. The classical-surface model was shaped as the TsAGI R-3a-12 airfoil [27,28]. In the case of the wavy-surface model, the airfoil was the same both along the grooves and the humps with the hump height $f = 2$ mm $(0.01c)$, see Fig. 3. In such a way, the paraglider wing was imitated. The maximum error in model manufacturing was smaller than 0.2 mm per 100 mm length. The surface roughness was less than 0.5 μm. All experiments were performed at the angle of attack $\alpha = 0$ deg. Both models were equipped with round end plates 220 mm in diameter and 2 mm thick.

C. Pressure-Distribution Measurement

The pressure distribution on the wing surface was measured by a static pressure probe 0.8 mm in diameter with a 0.4 mm pressure tap located 2 mm downstream of the probe tip. During the measurement, the probe orientation was kept constant to provide its contact with the model surface at the static pressure tap location. According to the preliminary experiments performed at $U_\infty = 12$ m/s on a pressure-tapped wing with 100 mm chord, the difference between the probe tap and wing pressure taps was no more than 5% of dynamic pressure q_∞ in the measurement range of 15–100% of the model chord. In this experiment, the pressure was measured by a differential pressure gauge Omega PX2650-10D5V (differential pressure transducer with a range of 0–10 in. H_2O with a 0.2–5.2 V output) as the difference between the total pressures p_0 measured by a pitot tube placed in the freestream upstream of the wing and by the aforementioned probe. The pressure coefficient was obtained as

$$c_p = (p - p_0)/q + 1 \tag{1}$$

The probe was moved with a computer-controlled traverse mechanism. The gauge signal was transmitted to the computer by an A/D converter, National Instruments PCI 6023.

D. Hot-Wire Measurements

The hot-wire data were obtained with an AN-1003 constant-temperature anemometer (AA Labs) and an I-type, single-wire, boundary-layer probe. The wire had a length of 2 mm and a diameter of 6 μm. It was calibrated with a pitot-static tube before each test. The anemometer signal was fed to a computer using a PCI 6023 board. The behavior of the velocity u with voltage E was defined as

$$u = k_1(E^2 - E_0^2)^{1/n} + k_2(E^2 - E_0^2)^{1/2} \tag{2}$$

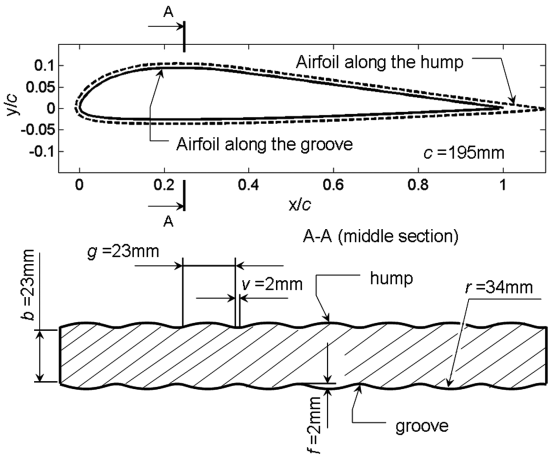

Fig. 3 Geometry of the wavy wing.

The second semi-empirical term of the equation takes into account free convection at low velocities and enables correct hot-wire measurements near the wall [29]. The mean and root-mean-square (rms) disturbance streamwise velocity components were determined at each measurement point by 20 samples with a duration of 0.5 s and sampling frequency of 2048 Hz. To obtain the disturbance spectral density, the location of the maximum amplitude of disturbances was chosen in the wall-normal rms disturbance profiles. In these cases, the sampling frequency was 10,000 Hz and the sample duration was 100 s. Bartlett's method [30] was used for signal processing.

III. Results and Discussion

A. Choosing Angle of Attack for Detailed Boundary-Layer Investigation

Oil-film visualization on the classical wing at a near-stall angle of attack $\alpha = 15$ deg showed that there is a three-dimensional flow structure in the aft part of the separation bubble (Fig. 4). At increasing angle of attack, stall is observed. At decreasing angle of attack, the boundary layer attaches at $\alpha = 14$ deg. On the wavy wing at $\alpha = 20$ deg, the separation bubbles are located only in the grooves (Fig. 5), and the flow behind the bubbles is attached over the entire wingspan. Under the conditions of the T-324 wind tunnel, the stall on the wavy wing occurs at $\alpha = 28$ deg. It was noted that the flow

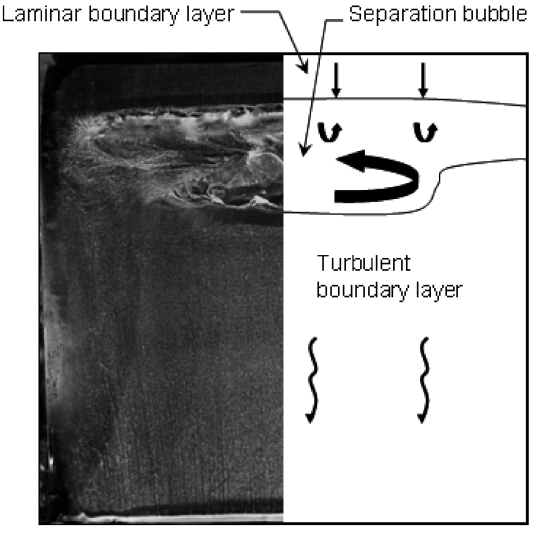

Fig. 4 Oil-film visualization and its interpretation for the classical wing at prestall angle of attack $\alpha = 15$ deg.

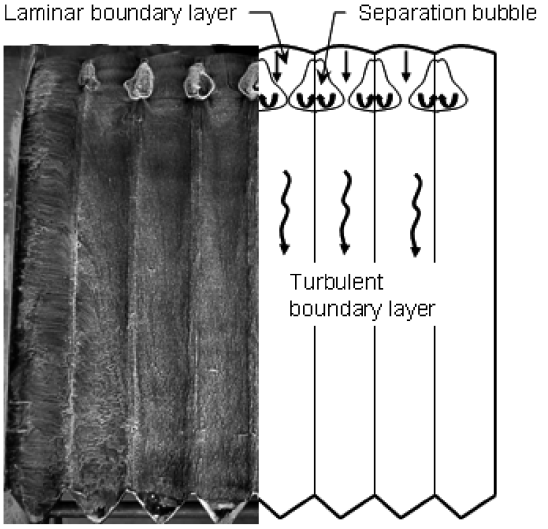

Fig. 5 Oil-film visualization and its interpretation for the wavy wing at angle of attack $\alpha = 20$ deg.

structure on both the classical and the wavy wings at an angle of attack $\alpha = 15$ deg, which is the near-critical angle for the classical wing, is similar to that at a zero angle of attack. In the latter case, however, the separation bubble has larger length and thickness (Figs. 6 and 7). This allows one to obtain detailed information about the flow structure in the separation region by other methods, for example, through hot-wire and pressure measurements. For that reason, the present investigation was performed at zero angle of attack.

B. Comparison of the Oil-Film Visualization Pattern with the Pressure Distribution

Acquisition of quantitative data on the flow velocity in the boundary layer over the whole wing surface with the hot-wire anemometry method is known to be time-consuming, especially over complex three-dimensional surfaces. Therefore, the hot-wire measurements in the present work were performed in several cross sections, which were selected by other methods. To determine the general pattern of the flow, two complementary methods characterizing the boundary-layer structure were used: oil-film visualization and pressure-distribution measurements. The oil-film patterns (Figs. 6 and 7) were taken from our previous work [25], in which the boundary-layer structure was studied on the classical and wavy wings at various angles of attack. Figures 6 and 7 and Table 1 characterize the section wherein the detailed hot-wire measurement was performed. The orthogonal coordinates were aligned in the streamwise direction X, normal-to-surface direction Y, and spanwise direction Z.

The oil-film visualization on the classical wing shows three typical flow regions: 1) the laminar boundary-layer region, which ends with a two-dimensional separation, 2) the separation-bubble region, which ends with a three-dimensional reattachment, and 3) the turbulent boundary layer (Fig. 6). On the wavy wing, the separation bubbles are localized only between the humps. It is rather difficult to determine where exactly the laminar-turbulent transition occurs for this flow geometry (Fig. 7).

The pressure-distribution curves along the wing chord are plotted in Fig. 8 for section numbers 1, 2, and 3. For section numbers 1 and 2, characterizing the separated flow, the key changes in the flow regime can be found with the help of the oil-film visualization and the data on the pressure distribution. These key locations are the separation point

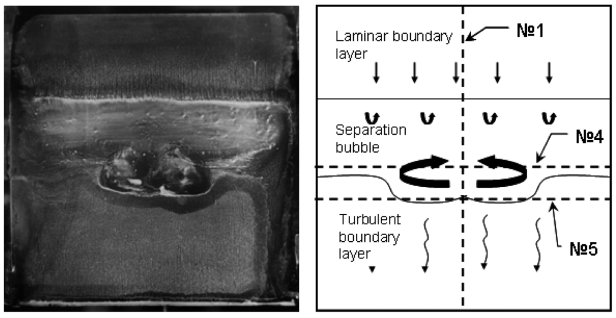

Fig. 6 Oil-film visualization and its interpretation for the classical wing at $\alpha = 0$ deg (dashed lines indicate hot-wire measurement sections).

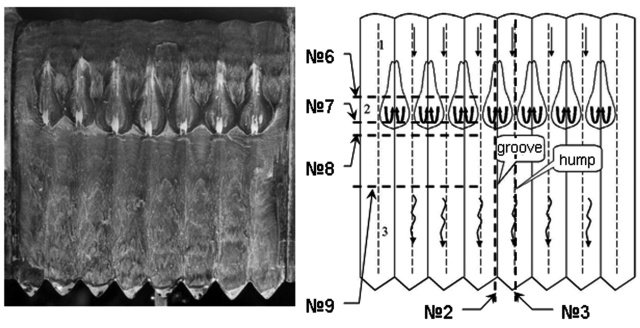

Fig. 7 Oil-film visualization and its interpretation for the wavy wing at $\alpha = 0$ deg (dashed lines indicate hot-wire measurement sections).

Table 1 Section position

Number of section	Model name	Plane	Position
1	Classical	XY	Along the symmetry axis
2	Wavy	XY	Along the groove
3	Wavy	XY	Along the hump
4	Classical	YZ	$0.538c$
5	Classical	YZ	$0.615c$
6	Wavy	YZ	$0.333c$
7	Wavy	YZ	$0.385c$
8	Wavy	YZ	$0.487c$
9	Wavy	YZ	$0.743c$

S, the transition point T, and the reattachment point R. The subscript indicates the type of wing model: classical wing (cl) and wavy wing (gr); in the latter case, the measurements are performed along the groove. Thus, it is obvious from Figs. 7 and 8 that no separation of the boundary layer occurs on the wavy-wing hump. To determine the transition, however, hot-wire measurements are necessary.

C. Hot-Wire Anemometry Measurements

Figure 9 shows the hot-wire mean and rms disturbance velocity profiles. The y shift between the groove and the hump profiles is equal to the hump height $f = 2$ mm. The shapes of the velocity profiles confirm a significant difference of the flow at the wavy-wing groove and hump. Some similarity to the classical wing is still seen in the groove, but there is a crucial difference on the hump. The disturbance growth is smaller in the hump region, as compared to the groove region and the classical wing. It is convenient to consider the similarities and the differences of the boundary layers using integrated parameters δ_1, δ_2, H_{21}, etc. The procedure of calculating the integrated parameters used for this purpose is described as follows.

1. Applying Green's Two-Parameter Profiles to Correct Hot-Wire Velocity Data

The inability of a single-wire anemometer to measure the direction of the velocity vector is its disadvantage. In our case, first, the flow has a three-dimensional structure and, second, reverse flows occur in the separation-bubble region. Hence, the velocity profiles are distorted near the wing surface. The effect of the three-dimensional flow on hot-wire measurements was reduced by performing the measurements in the plane of symmetry of the three-dimensional structures, where the flow can be considered as locally two-dimensional. The influence of the reverse flow on determining the displacement thickness and momentum thickness was reduced by approximating the experimental profiles in the separation region through analyzing Green's profiles [31].

Green's two-parameter velocity profiles [31] were constructed to model the turbulent reattachment in a wake region. In the flowfield of

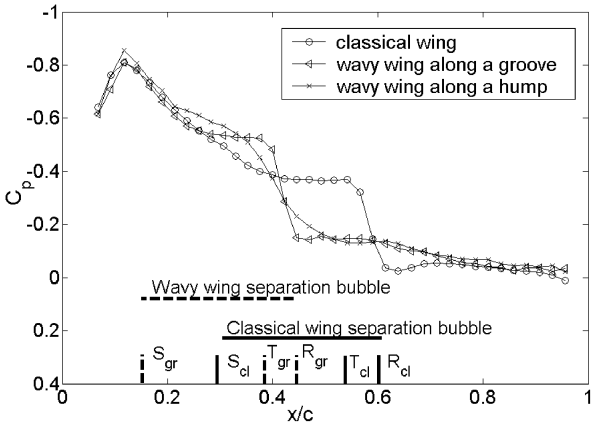

Fig. 8 Pressure distributions along the wing chord and key points of the flow structure.

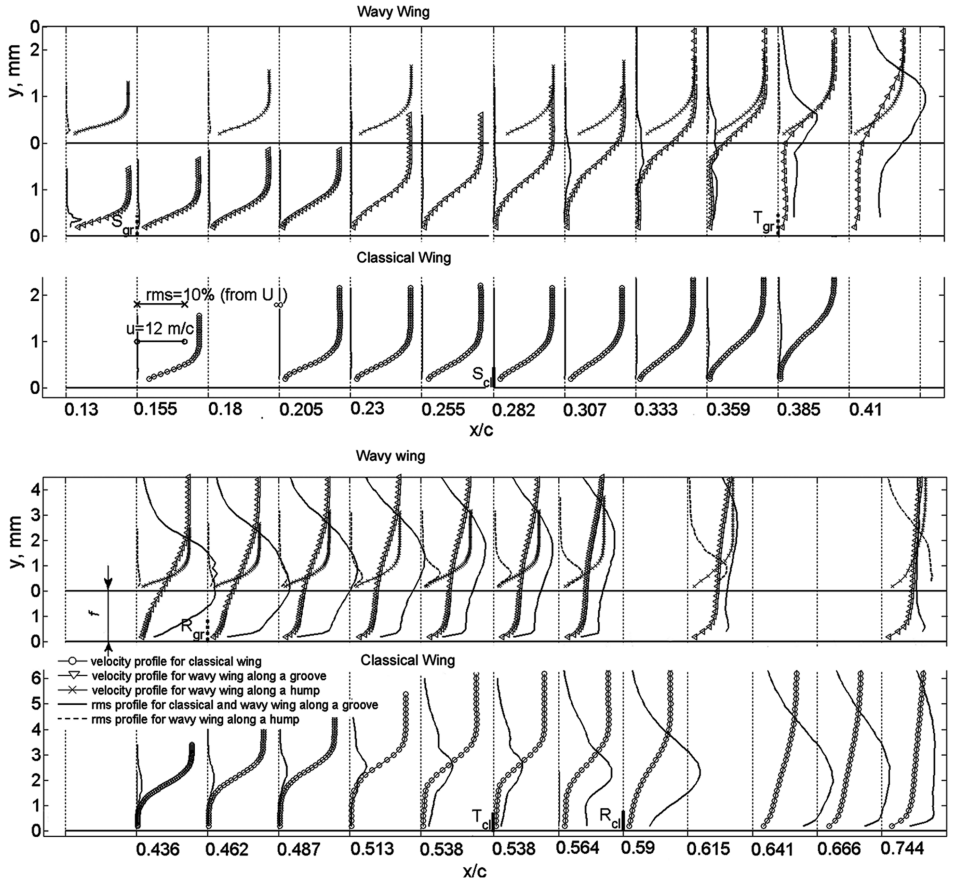

Fig. 9 Comparison of measured mean and rms disturbance velocity profiles along the chord for the classical and wavy wings.

Green's model, velocity profiles downstream of the reattachment point were represented by Cole's family of wake velocity profiles. Velocity profiles upstream of the reattachment point were represented by a constant velocity region bounded with a (separated) shear layer. The resultant profile is shown in Fig. 10 (dotted curve). Such profiles are based on the parameter P from Cole's family of profiles and on the parameter h (often nondimensionalized by the shear-layer thickness l), which defines the distance between the surface (in Green's case, the wake centerline) and the shear layer. The velocity distribution is

$$u/U_\infty = 1 - 2P$$

for $0 \le y \le h$ and

$$u/U_\infty = 1 - P\left[1 + \cos\left(\pi \frac{y-h}{\ell}\right)\right]$$

for $h \le y \le (h + l)$. Note that the defined "shear layer" (of length l) extends below y_0 (where $u = 0$) for these profiles (cited from [8]).

Green's family of profiles [31] was considered suitable to simulate the boundary-layer velocity profile in the separation-bubble region [8]. Fitzgerald and Mueller [8] compared Green's profiles with the data obtained by means of laser Doppler velocimetry (LDV) measurements, which were capable of determining the velocity direction. Using a fairly simple method of parameter definition, they obtained good agreement between the velocity values [8]. To specify the parameters P and h within the separation-bubble region, they used simple linear dependences, which were derived, however, on

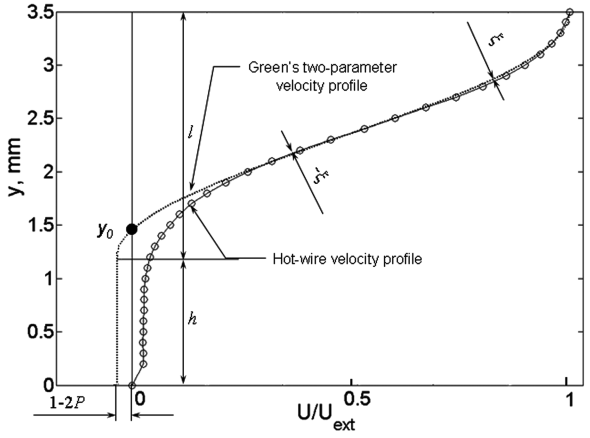

Fig. 10 Green's two-parameter velocity profile used instead of the measured one.

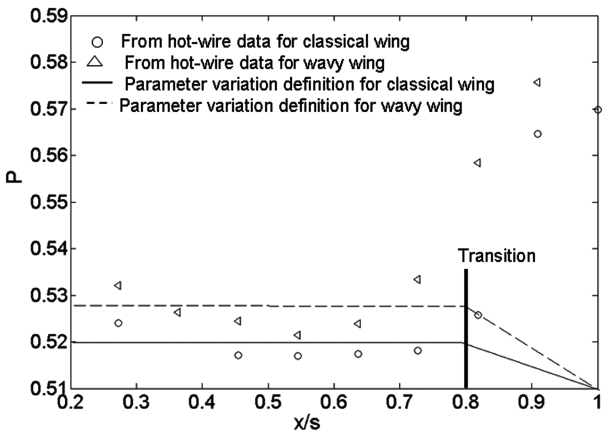

Fig. 11 Variation of P with the bubble length s determined through hot-wire data.

the basis of the LDV data on the reverse flow in the separation bubble.

In the present paper, the parameters P and h were estimated from hot-wire measurements. In the laminar part of the separation bubble, the absolute value of the reverse-flow velocity was assumed to be equal to that at a point with $dU/dy \approx 0$ on the experimental profile (Fig. 10). Figure 11 shows the values of P calculated under this assumption. To select the analytical profiles, we used a simple dependence of P on the bubble length s (solid curve in Fig. 11). It should be noted that this dependence for the classical wing coincides exactly with that proposed by Fitzgerald and Mueller [8], which corresponds to a reverse flow with the absolute value of velocity approximately equal to 4% of U_{ext}. For the flowfield along the groove, the parameter P was chosen to be slightly higher, which corresponds to the reverse-flow velocity of about 5% of U_{ext}. In [8], the LDV-measured profiles were in good agreement with Green's family of profiles. For this reason, the parameter l was chosen to ensure the minimum deviation ξ between the experimental and Green's profiles in the section $0.3U_{ext} \le u \le 0.99U_{ext}$. An example of such fitting is shown in Fig. 10. The ratio h/l is plotted in Fig. 12 as a function of the bubble length s. It should be noted that such a selection gives the discrepancy value ξ of about 1.5% of U_{ext} in the laminar part of the separation bubble; after the transition, the discrepancy increases to 7% of U_{ext}.

2. *Integral Boundary-Layer Characteristics*

The integral boundary-layer parameters and the shape factors were calculated after the experimental profiles obtained in the separation region were replaced with Green's profiles. If the reverse flow is ignored, the error in the displacement-thickness estimates may reach 10 and 15% for the classical and wavy wings, respectively, and the error in the momentum thickness is 120 and 200%, respectively. Similar results for the separation-bubble flowfield were obtained in [8].

The integral boundary-layer parameters δ_1, δ_2, and δ_3 versus the chord length are shown in Fig. 13. The curve shapes are fairly similar for the classical wing and for the wavy wing along the groove and are typical for the separation-bubble flowfield at low Reynolds numbers. The bubble lengths on the wavy-wing groove and on the classical wing are almost identical; after separation, however, the displacement thickness grows slower along the groove than on the classical wing. On the other hand, the momentum thickness for the groove is smaller than for the classical wing before the transition. It is clearly seen that all processes in the wavy-wing groove start at 15% of the chord, which is earlier than in the classical-wing case. The flow on the wavy-wing hump is attached; hence, the integral boundary-layer parameters behave differently. At a distance of 0.6 of the chord, the intense growth of the integral boundary-layer parameters along the groove is finished as the turbulent boundary-layer parameters are reached. At the same time, the parameters on the hump only start growing, and the transition does not seem to be finished at 0.74 of the chord, where the last measurement was performed.

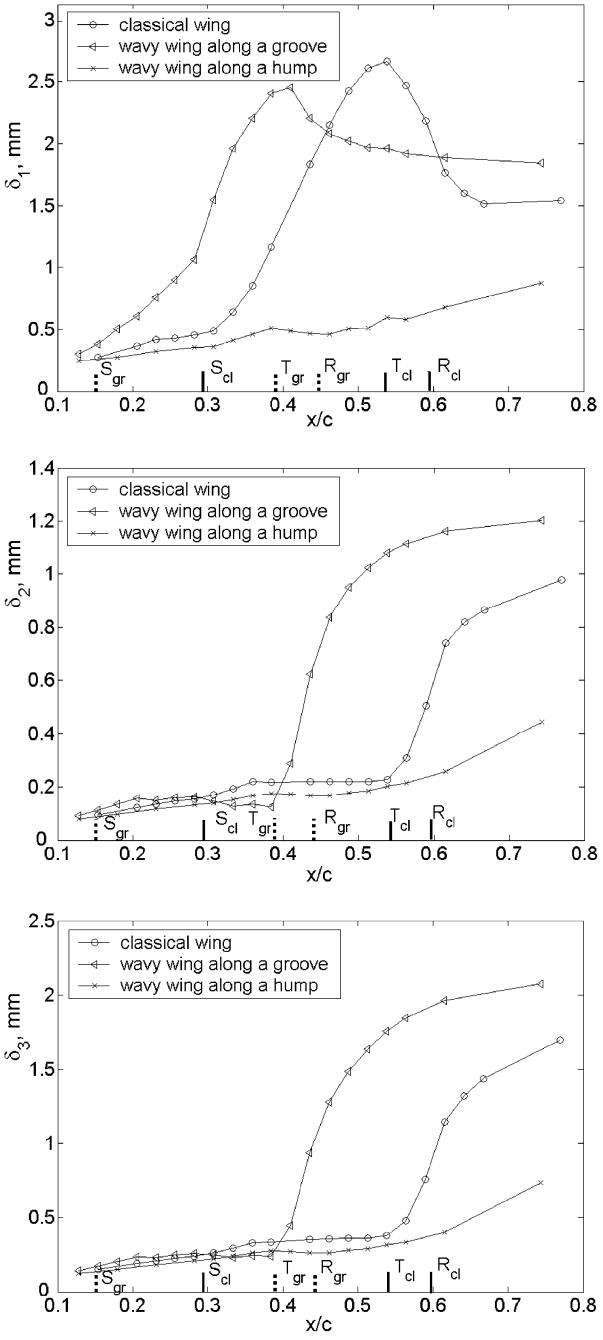

Fig. 13 Comparison of integral boundary-layer parameters.

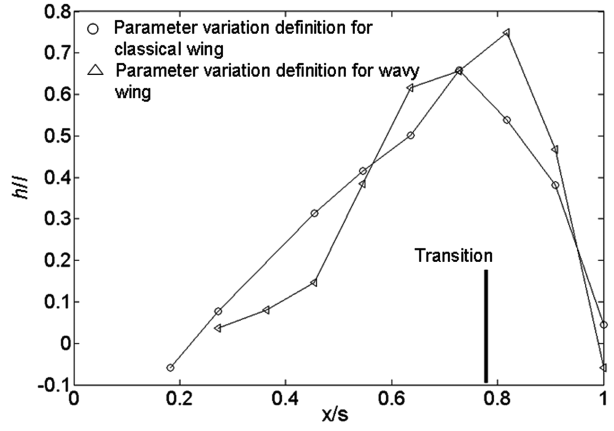

Fig. 12 Variations of h/l with bubble length s obtained by the approximation.

The difference between the boundary-layer structure on the hump and in the groove is also evidenced by the changes in the shape factors H_{21} and H_{32} (Fig. 14). Along the groove, the shape factor H_{21} has a maximum at the transition point, which is typical for the separated flow, and H_{32} has a typical minimum in the reattachment region. Along the hump, H_{21} and H_{32} change weakly, and it is only at 74% of the chord that H_{21} and H_{32} approach values typical for the turbulent boundary layer.

3. *Transitions on Classical and Wavy Wings*

The solid and dashed curves in Fig. 9 show the disturbance profiles. The data in Fig. 15 illustrate the rms disturbance growth along the line passing through the disturbance profile maxima presented in Fig. 9. Some similarity is observed in the development of disturbances in the separation region on the classical and wavy wings. In both cases, the disturbances grow slowly, immediately

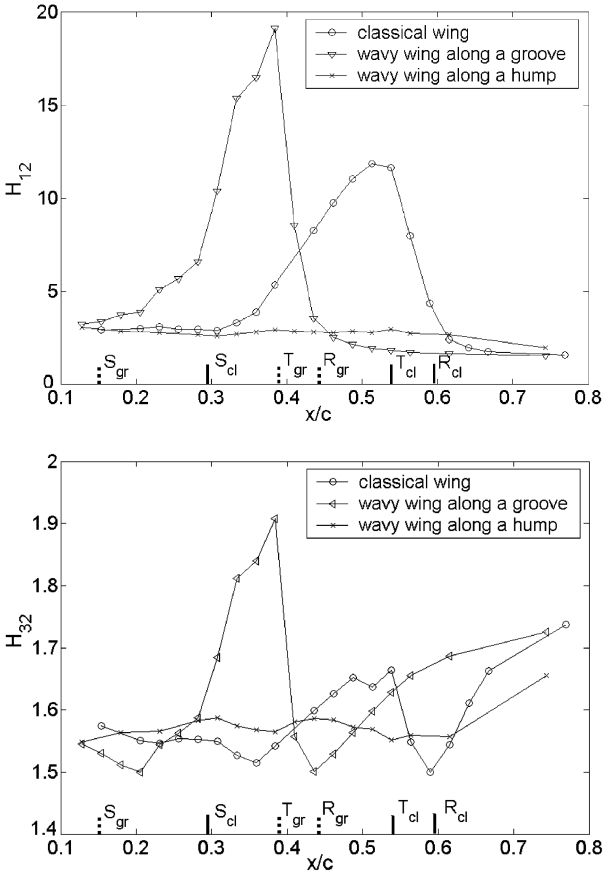

Fig. 14 Comparison of shape factors.

behind the laminar separation. After that, however, intensive nonlinear growth is observed, which is faster in the separation region on the wavy wing.

Two important features in Fig. 15 are worth noting. The first one is the high level of disturbances near the leading edge along the wavy-wing groove, which is later reduced. The second one is insignificant growth of disturbances on the hump, whereas the transition in the groove is very intense and the disturbances start decaying at 0.5 of the chord. Apparently, the disturbances on the hump did not yet reach their maximum at 0.74 of the chord. Together with the distributions of the integral parameters, this fact indicates that the transition on the hump is not completed at 0.74 of the chord.

The results of the spectral analysis of disturbances are shown in Fig. 16 as power spectra densities (PSD) for the classical and wavy wings. The disturbances initially behave similarly along the classical wing and the wavy-wing groove. This similarity is manifested in the

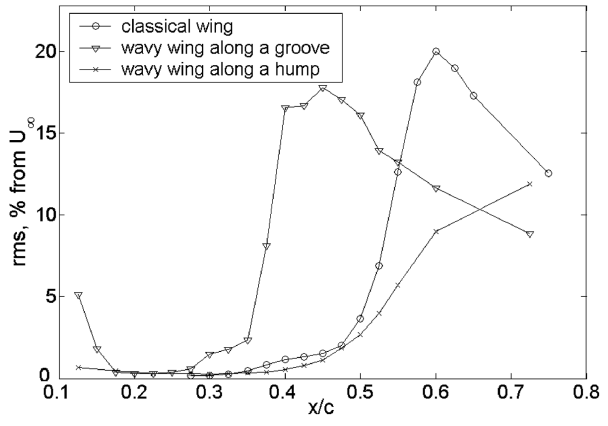

Fig. 15 Streamwise disturbance growth.

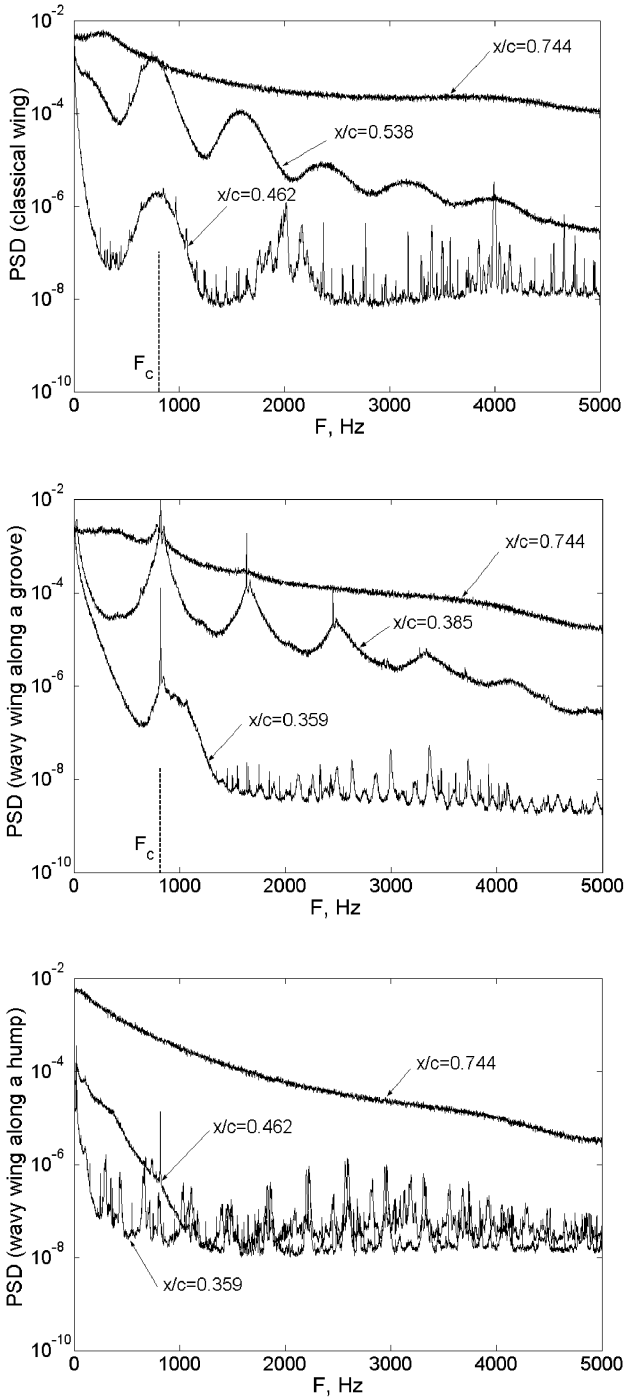

Fig. 16 Disturbance spectra at rms maxima of the boundary-layer perturbations.

development of exponentially growing instability wave packets with the central frequency $F_c = 800$ Hz. A corresponding local stability analysis was performed for the classical and wavy wings [32,33]. The experimental velocity profiles were approximated by a spline function and were analyzed within the framework of the linear stability theory. For the wavy wing, the approach within the framework of the locally parallel flow approximation may not be exactly appropriate, nevertheless, such calculations were performed because the velocity profiles were measured along the axis of symmetry of the local separation bubble, where the flow is assumed to be quasi-two-dimensional. The results showed that the frequency and growth rate of the most unstable disturbances at the initial stage of the transition to turbulence are in good agreement with the experimental results in the separation region of both the classical and the wavy wings. The Strouhal number

$$St = F_c \delta_2 / U_{\text{ext}}$$

was $St = 0.0108$ for the classical wing and $St = 0.0093$ for the wavy wing. These values are lower than those for free shear layers, where the Strouhal number usually exceeds 0.016 [34]. The stage of nonlinear growth of disturbances is clearly seen in the spectra. The nonlinearity is manifested in growing of spectral frequency harmonics, which are multiple to the central frequency F_c of the initial wave packet (see the spectra for 0.538 of the chord for the classical wing and for 0.385 of the chord for the wavy wing). This nonlinear stage proceeds faster on the wavy wing. Further downstream, the spectrum is filled uniformly, which testifies that the flow becomes turbulent. Along the hump, no pronounced wave packets are observed, the spectrum being filled at a more downstream position than that along the groove.

4. *Hot-Wire Measurements Along the Wingspan*

The aforementioned investigations allowed us to conclude that the boundary-layer structures on the hump and in the groove differ essentially. The hot-wire measurements, which were performed in cross sections 6, 7, 8, and 9 (see Table 1 and Figs. 6 and 7), characterize the distribution of disturbance between the hump and the groove. The measurements in cross sections 4 and 5 show the influence of the three-dimensional structure in the region of the separated boundary-layer reattachment on the classical wing.

Figure 17a shows the rms disturbance contours in the classical-wing boundary layer at 0.538 of the chord. The maximum disturbance amplitude is observed exactly above the left and right parts of the three-dimensional structures observed on the oil-film visualization pattern in the aft part of the separation bubble (see Fig. 6). The difference in the disturbance amplitude

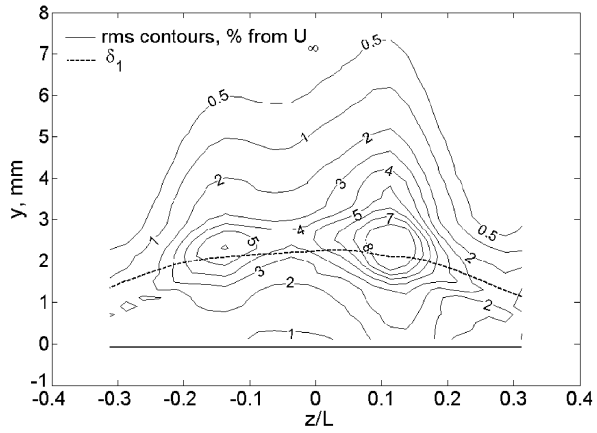

a) x/c=0.538

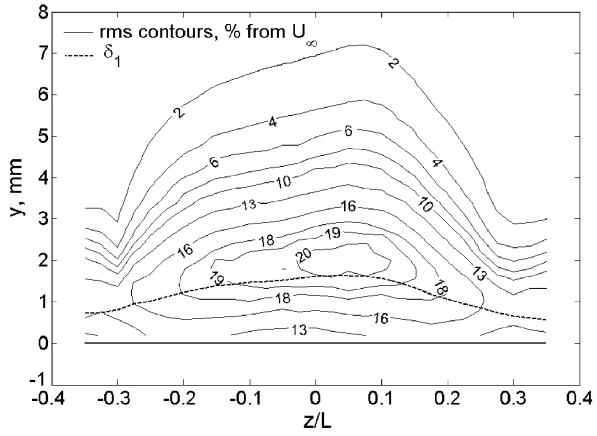

b) x/c=0.615

Fig. 17 Rms disturbance distribution in the spanwise direction on the classical wing.

at an identical distance from the surface can reach 80% of the maximum disturbance amplitude in this section. Further downstream, however, the disturbances rapidly spread in the spanwise direction, and the difference in the disturbance amplitude in the boundary-layer reattachment region, which appears at 0.615 of the chord, decreases to 35% of the maximum disturbance value in this section (Fig. 17b).

As the oil-film visualization indicated the presence of a periodic flow in the spanwise direction on the wavy wing, the area of hot-wire measurements covered only one and a half surface waves in the spanwise direction. The rms disturbance distributions over the wavy wingspan are plotted in Fig. 18. The displacement thickness is shown with the dotted curve. In this case, the displacement thickness was calculated directly from the hot-wire measurement data; hence, its value in the separation region can be underestimated (but by no more than 15%). The probe wire orientation was always horizontal; therefore, the measurements near the hump slope also involved some error. The qualitative pattern of the rms disturbance distribution, however, is not affected by these errors.

For example, cross section 6 (Fig. 18a) clearly shows that the maximum disturbance amplitude appears near the hump slope. Further downstream, the disturbance maximum is shifted to the groove center (Fig. 18b). In the transition region above the separation bubble (Fig. 18b), the difference in disturbance amplitudes reaches 90% of the maximum amplitude in this section. After the reattachment, this difference persists, in contrast to the classical-wing case (Fig. 18c). Further downstream, the disturbances become attenuated along the groove, but their spanwise propagation is rather limited. More pronounced spreading of the disturbances in the spanwise direction is observed at the hump tip (Fig. 18d).

IV. Further Comments

It is important that there is a three-dimensional structure in the aft part of the separation bubble on the classical wing. This structure may be expected to form owing to the influence of the end plates. The separation line, however, is not affected. Moreover, additional oil-film visualizations in other subsonic wind tunnels, where the natural freestream turbulence level reaches $Tu = 0.7\%$, did not display any three-dimensional structures in the aft part of the separation bubble, that is, the reattachment line was straight. At a low turbulence level ($Tu = 0.04\%$), according to our research, the three-dimensional structure is registered not only by means of the oil-film visualization but also with the hot-wire measurements. It is manifested as two pronounced maxima in the spanwise rms distributions, exactly above the structures found with the oil-film visualization. In general, according to the measurements along the classical-wing chord, the boundary-layer structure and the transition position agree with the classical concept [3–5].

For the wavy wing, which has no air inlets, most of the results are new. In Babinsky's works [17,18], the oil-film visualization was performed for the wing with air inlets at the leading edge, while the Reynolds numbers were 5–7 times higher than they are in this work. Fish and Battle [19], Watts and Fish [20], Fish and Lauder [21], and Miklosovic et al. [22] investigated the flow around the wing with a wavy leading edge and with no air inlets by means of numerical simulations and wind-tunnel measurements. These investigations showed the positive influence of the wavy surface: a higher critical angle of attack and a higher lift-to-drag ratio. The numerical data on the surface pressure distribution of the wavy (humpback) wing [20], however, do not correlate with the experimental results given in this paper. In [20,24], the minimum pressure was found in the groove, whereas, in our experiments, it is observed on the hump.

On the other hand, the measurements of Johari et al. [23] validated only an increase in the critical angle of attack and flattening of the lift curve for the wing with a wavy leading edge, as compared with the classical wing.

In our opinion, this scatter in results can hardly be explained without understanding the detailed flow pattern in the boundary layer. The scenario of the leading-edge stall on the classical wing affects the results of comparisons with the wavy wing. If the

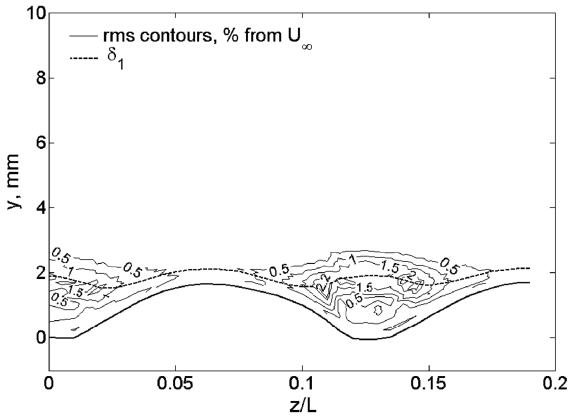

a) $x/c=0.333$

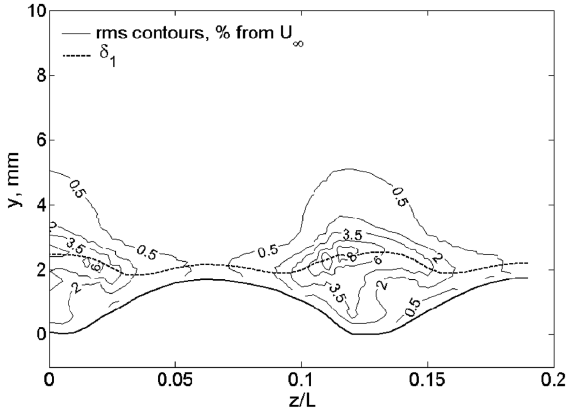

b) $x/c=0.385$

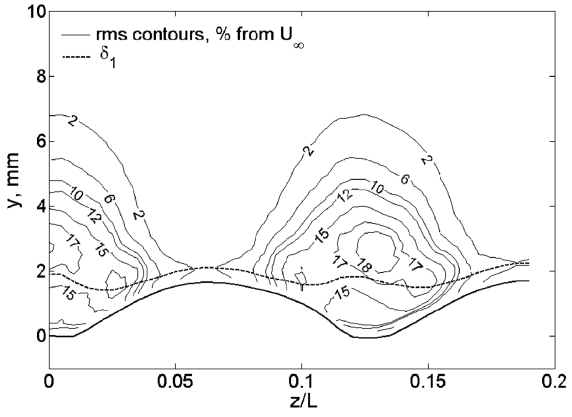

c) $x/c=0.487$

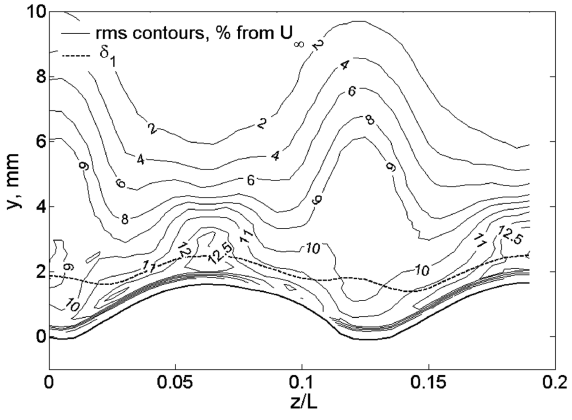

d) $x/c=0.744$

Fig. 18 Rms disturbance distribution in the spanwise direction on the wavy wing at 0.744 of the chord length.

boundary layer is assumed to be already turbulent on the leading-edge, Johari et al.'s approach on the tuft visualization [23] of the flow pattern on the wing surface seems to be justified. In this case, the calculation method proposed by van Nierop et al. [24], which offers an explanation for the flattening of the lift curve for the wing with a wavy leading edge, also seems to be suitable.

If there is an extended laminar flow region and a separation bubble on the wing, which is typical for Reynolds numbers lower than 2×10^5 and low freestream turbulence, it is necessary to consider the influence of the wavy surface on the boundary-layer structure in the separation-bubble region. By preventing the separation-bubble from bursting, it is possible to increase not only the critical angle of attack but also the maximum lift.

V. Conclusions

The boundary layer on the top surface of the classical and wavy wings at an angle of attack $\alpha = 0$ deg was investigated. The oil-film visualization, pressure-distribution measurements by means of a static pressure miniprobe, and hot-wire measurements were performed. These techniques complement each other.

The data obtained by means of the hot-wire measurements in the separation-bubble region were corrected by a novel approach using only the hot-wire data. The integral boundary-layer characteristics based on the corrected hot-wire data are in qualitative agreement with the data of the study [8], where they were obtained by the LDV method. In particular, this agreement implies a correct behavior of the shape factor H_{23}, which reaches its maximum in the transition region and has a local minimum in the reattachment region.

We managed to find common features in the separation bubbles on the classical and wavy wings. In the laminar part of the separation bubbles, the disturbances behave similarly: they appear as amplifying wave packets of small-amplitude shear-layer perturbations. The following difference was found between the flow configurations: on the wavy wing, the central frequency F_c of the packet is more pronounced in the grooves, and the disturbances at the nonlinear stage of the transition to turbulence grow faster than in the separated flow of the classical wing.

At a low freestream turbulence level ($Tu = 0.04\%$), a three-dimensional flow structure appears in the aft part of the separation bubble of the classical wing. Because of these structures, the rms disturbance distributions above the aft part of the separation bubble are nonuniform. When the boundary layer reattaches, however, this nonuniformity disappears.

An essentially different structure of the boundary layer was observed along the groove and the hump of the wavy wing. On the hump, the laminar-turbulent transition begins at 30% of the chord downstream, as compared with the groove. The transition scenarios along the groove and hump are also different. On the hump, the transition occurs without flow separation and generation of a pronounced instability wave packet.

Obviously, the spanwise pressure gradients, which arise on the leading edge of the wavy wing, form a complex three-dimensional structure of the boundary layer; the laminar separation in the groove occurs earlier than on the classical wing, and there is no separation on the hump. The boundary layer with such a structure may experience high positive pressure gradients without turbulent boundary-layer separation or bubble bursting. Thus, we assume that the maximum lift and the critical angle of attack can be increased in flows with Reynolds numbers lower than 2×10^5 by making the wing surface wavy in the spanwise direction.

Further investigations of the boundary layer of the wavy wing are expected to provide the possibility of optimizing the geometric parameters of the wavy surface and improving the wing performance at low Reynolds numbers.

Acknowledgments

This work is supported by the Ministry of Education and Science of the Russian Federation (grant no. RNP.2.1.2.3370), Russian Foundation for Basic Research (grant no. 08-01-00027), and the

Grant of the Russian Federation for scientific schools (grant no. NSh-454.2008.1). The authors also wish to acknowledge Andrei Boiko and Alexander Dovgal for their helpful suggestions in the manuscript preparation.

References

[1] Coppinger, R., "Down Sizing," *Flight International*, Vol. 168, No. 5008, Oct. 2005, pp. 32–34.

[2] Mueller, T. G. (ed.), *Fixed and Flapping Wing Aerodynamics for Micro Air Vehicle Applications*, Progress in Astronautics and Aeronautics, Vol. 195, AIAA, Reston, VA, 2001.

[3] Carmichael, B. H., "Low Reynolds Number Airfoil Survey," Vol. 1, NASA CR 165803, Nov. 1981.

[4] Ward, J. W., "The Behavior and Effects of Laminar Separation Bubbles on Aerofoils in Incompressible Flow," *Journal of the Royal Aeronautical Society*, Vol. 67, Dec. 1963, pp. 783–790.

[5] Horton, H. P., "Laminar Separation Bubbles in Two- and Three-Dimensional Incompressible Flow," Ph.D. Thesis, Univ. of London, London, 1968.

[6] O'Meara, M. M., and Mueller, T. J., "Laminar Separation Bubble Characteristics on an Airfoil at Low Reynolds Numbers," *AIAA Journal*, Vol. 25, No. 8, 1987, pp. 1033–1041. doi:10.2514/3.9739

[7] Brendel, M., and Mueller, T. J., "Boundary Layer Measurements on an Airfoil at Low Reynolds Numbers," *Journal of Aircraft*, Vol. 25, No. 7, 1988, pp. 612–617. doi:10.2514/3.45631

[8] Fitzgerald, E. J., and Mueller, T. J., "Measurements in a Separation Bubble on an Airfoil Using Laser Velocimetry," *AIAA Journal*, Vol. 28, No. 4, 1990, pp. 584–592. doi:10.2514/3.10433

[9] Dikovskaya, N. D., and Zanin B. Yu., "Flow Stability Investigation upon Windward and Leeward Wing Surface," *Thermophysics and Aeromechanics*, Vol. 7, No. 2, 2000, pp. 201–208.

[10] Drela, M., "XFOIL: An Analysis and Design System for Low Reynolds Number Airfoils," *Conference on Low Reynolds Number Airfoil Aerodynamics*, Univ. of Notre Dame, South Bend, IN, June 1989.

[11] Drela, M., and Giles, M. B., "Viscous-Inviscid Analysis of Transonic and Low Reynolds Number Airfoils," *AIAA Journal*, Vol. 25, No. 10, 1987, pp. 1347–1355. doi:10.2514/3.9789

[12] Bippes, H., "Experimental Investigation of Topological Structures in Three-Dimensional Separated Flow," *Boundary-Layer Separation*, edited by F. T. Smith, and S. N. Brown, Springer–Verlag, Berlin, 1987, pp. 379–382.

[13] Tobak, M., and Peak, D. J., "Topology of Three-Dimensional Separated Flows," *Annual Review of Fluid Mechanics*, Vol. 14, Jan. 1982, pp. 61–85. doi:10.1146/annurev.fl.14.010182.000425

[14] Dallman, U., "Topological Structures of Three-Dimensional Vortex Flow Separation," *AIAA 16th Fluid and Plasma Dynamics Conference*, AIAA 83-1935, 1983.

[15] Boiko, A. V., Dovgal, A. V., Zanin, B. U., and Kozlov, V. V., "The Space Structure of the Detached Flows on the Wings Profiles (Review)," *Thermophysics and Aeromechanics*, Vol. 3, No. 1, 1996, pp. 1–14.

[16] Zanin, B. U., Kozlov, V. V., and Mavrin, O. V., "About the Ways of the Global Stalling Control," *Thermophysics and Aeromechanics*, Vol. 4, No. 4, 1997, pp. 381–385.

[17] Babinsky, H., "Aerodynamic Improvements of Paraglider Performance," *17th AIAA Applied Aerodynamics Conference*, AIAA Paper 99-3148, 1999.

[18] Babinsky, H., "The Aerodynamic Performance of Paragliders," *The Aeronautical Journal*, Vol. 103, No. 1027, 1999, pp. 421–428.

[19] Fish, F. E., and Battle, J. M., "Hydrodynamic Design of the Humpback Whale Flipper," *Journal of Morphology*, Vol. 225, July 1995, pp. 51–60. doi:10.1002/jmor.1052250105

[20] Watts, P., and Fish, F. E., "The Influence of Passive, Leading Edge Tubercles on Wing Performance," *Proceedings of the Twelfth International Symposium on Unmanned Untethered Submersible Technology (UUST), UUST01*, Autonomous Undersea Systems Inst., Lee, NH, Aug. 2001.

[21] Fish, F. E., and Lauder, G. V., "Passive and Active Flow Control by Swimming Fishes and Mammals," *Annual Review Fluid Mechanics*, Vol. 38, Jan. 2006, pp. 193–224. doi:10.1146/annurev.fluid.38.050304.092201

[22] Miklosovic, D. S., Murray, M. M., Howle, L. E., and Fish, F. E., "Leading-Edge Tubercles Delay on Humpback Whale (Megaptera Novaeangliae) Flippers," *Physics of Fluids*, Vol. 16, No. 5, 2004, pp. L39–L42. doi:10.1063/1.1688341

[23] Johari, H., Henoch, C., Custudio, D., and Levshin, A., "Effects of Leading-Edge Protuberances on airfoil Performance," *AIAA Journal*, Vol. 45, No. 11, 2007, pp. 2634–2642. doi:10.2514/1.28497

[24] Van Nierop, E. A., Alben, S., and Brenner, M. P., "How Bumps on Whale Flippers Delay Stall: An Aerodynamic Model," *Physical Review Letters*, Vol. 100, Feb. 2008, p. 054502. doi:10.1103/PhysRevLett.100.054502

[25] Zverkov, I. D., and Zanin, B. Yu., "Wing Form Effect on Flow Separation," *Thermophysics and Aeromechanics*, Vol. 10, No. 2, 2003, pp. 197–204.

[26] Demin, V. C., Morin, O. V., Polyakov, N. F., and Sherbakov, V. A., "Low Disturbance Level Measurements by Hot-Wire," *Proceedings of the Siberian Branch of Academy of Sciences USSR*, Vol. 2, Technical Science Series, No. 8, 1972 (in Russian).

[27] Krasilshikov, P. P., *Airfoil Characteristics Atlas*, TsAGI, Moscow, 1940 (in Russian).

[28] "TSAGI_R_3A.dat," *UIUC Airfoil Coordinates Database* [online database], http://www.ae.uiuc.edu/m-selig/ads/coord_database.html#TSAGI [cited 19 March 2008].

[29] Johansson, A. V., and Alfredsson, P. H., "On the Structure of Turbulent Channel Flow," *Journal of Fluid Mechanics*, Vol. 122, April 1982, pp. 295–314. doi:10.1017/S0022112082002225

[30] Hayes, M. H., *Statistical Digital Signal Processing and Modeling*, Wiley, New York, 1996.

[31] Green, J. E., "Two-Dimensional Turbulent Reattachment as a Boundary-Layer Problem," AGARD CP 4, Pt. 1, 1966.

[32] Kozlov, V. V., Zverkov, I. D., Zanin, B. Yu., Dovgal, A. V., Rudyak, V. Ya., Bord, E. G., and Kranchev, D. F., "An Experimental and Theoretical Investigation Boundary Layer Disturbances Growth upon Low Aspect Ratio Wing," *Thermophysics and Aeromechanics*, Vol. 13, No. 4, 2006, pp. 551–560.

[33] Kozlov, V. V., Zverkov, I. D., Zanin, B. Yu., Dovgal, A. V., Rudyak, V. Ya., Bord, E. G., and Kranchev, D. F., "Development of Laminar-Separating-Flow Perturbations on a Wavy Wing," *Thermophysics and Aeromechanics*, Vol. 14, No. 3, 2007, pp. 329–326.

[34] Ho, C. M., and Huerre, P., "Perturbed Free Shear Layers," *Annual Review Fluid Mechanics*, Vol. 16, Jan. 1984, pp. 365–424. doi:10.1146/annurev.fl.16.010184.002053

J. Wei
Associate Editor